ORIGINAL ARTICLE

ACTA RADIOLOGICA

Comparison of Gd-DTPA-Induced Signal Enhancements in Rat Brain C6 Glioma among Different Pulse Sequences in 3-Tesla Magnetic Resonance Imaging

H. SATO, J. ENMI, N. TERAMOTO, T. HAYASHI, A. YAMAMOTO, T. TSUJI, H. NAITO & H. IIDA

Laboratory for Diagnostic Solutions and Department of Investigative Radiology, Advanced Medical Engineering Center, Research Institute, National Cardiovascular Center, Osaka, Japan; Diagnostic Imaging Medical Affairs, Medical Affairs, Product Development Department, Bayer Yakuhin, Ltd., Osaka, Japan; Department of Radiology, Hospital of National Cardiovascular Center, Osaka, Japan

Sato H, Enmi J, Teramoto N, Hayashi T, Yamamoto A, Tsuji T, Naito H, Iida H. Comparison of gd-dtpa-induced signal enhancements in rat brain c6 glioma among different pulse sequences in 3-tesla magnetic resonance imaging. Acta Radiol 2007;000:1–8.

Background: T1-shortening contrast media are routinely used in magnetic resonance (MR) examinations for the diagnosis of brain tumors. Although some studies show a benefit of 3 Tesla (T) compared to 1.5T in delineation of brain tumors using contrast media, it is unclear which pulse sequences are optimal.

Purpose: To compare gadopentetate dimeglumine (Gd-DTPA)-induced signal enhancements in rat brain C6 glioma in the thalamus region among different pulse sequences in 3T MR imaging.

Material and Methods: Five rats with a surgically implanted C6 glioma in their thalamus were examined. T1-weighted brain images of the five rats were acquired before and after Gd-DTPA administration (0.1 mmol/kg) using three clinically available pulse sequences (spin echo [SE], fast SE [FSE], fast spoiled gradient echo [FSPGR]) at 3T. Signal enhancement in the glioma (E_T) was calculated as the signal intensity after Gd-DTPA administration scaled by that before administration. Pulse sequences were compared using the Tukey-Kramer test.

Results: E_T was 1.12 ± 0.05 for FSE, 1.26 ± 0.11 for FSPGR, and 1.20 ± 0.11 for SE. FSPGR showed significantly higher signal enhancement than FSE and comparable enhancement to SE.

Conclusion: FSPGR is superior to FSE and comparable to SE in its ability to delineate rat brain C6 glioma in the thalamus region.

Key words: Brain; contrast agents; MR imaging

Hiroshi Sato, Laboratory for Diagnostic Solutions, Advanced Medical Engineering Center, Research Institute, National Cardiovascular Center, 5-7-1 Fujishiro-dai, Suita, Osaka 565-8565, Japan (fax. +81 6 6835 5429, e-mail. cano@ri.ncvc.go.jp)

Accepted for publication August 5, 2007

T1-shortening contrast media are routinely used in magnetic resonance (MR) examinations for the diagnosis of brain tumors. Some studies show a benefit of 3 Tesla (T) compared to 1.5T in delineation of brain tumors using contrast media (1–5). However, it is unclear which pulse sequences are optimal. The conventional spin-echo (SE) technique has been most frequently used for T1-weighted (T1W) imaging of tumors after contrast media administration. The gradient-echo (GRE) technique, which is faster than SE, was introduced initially at 1.5T or lower field strength (6–11). Some studies have reported that GRE techniques compare favorably with the SE technique for delineation of brain tumors (8–10), while other studies have reported that GRE techniques do not show contrast enhancement as well as SE (6, 7, 11). At 3T, as at 1.5T or lower field strength, the issue of whether GRE techniques are effective compared to SE has not been determined. In 16 patients, NÖBAUER-HUMANN et al. reported that 3D GRE with magnetization preparation (MPRAGE) was comparable to T1W SE in tumor-to-brain contrast at 3T, although the parameters of T1W SE were not

informa
healthcare

DOI 10.1080/02841850701630326

optimized for 3T (1). In 12 patients, FISCHBACH et al. compared four T1W sequences: SE, inversion recovery fast SE (IR-FSE), 2D GRE, and MPRAGE at 3T. They observed that SE and IR-FSE provided higher contrast enhancement of brain tumors than 2D GRE and MPRAGE. Furthermore, their impressions showed that the visual quality of SE was superior to that of the other three sequences (12).

In order to compare pulse sequences, it would be preferable if the pathological and physiological conditions of subjects were constant across scans. One possible model system is the widely used rat brain glioma model (4, 5, 13–15). In most studies with small animals, MR imaging systems with small magnets are widely used. The pulse sequences available on the scanner designed for small animals, however, are different from those on a clinical scanner. By using a scanner designed for humans, we can compare diagnostic values of practical clinical pulse sequences. To our knowledge, no studies have been reported comparing pulse sequences on a 3T human scanner using a rat brain glioma model.

The purpose of the current study was to elucidate the optimal pulse sequence that provides the highest obtainable signal enhancement using gadopentetate dimeglumine (Gd-DTPA) in a rat brain C6 glioma model on a 3T human whole-body scanner.

Material and Methods

Protocols of all animal procedures were approved by the ethics committee for animal research at the National Cardiovascular Center. Male Sprague-Dawley rats (Japan SLC, Inc., Shizuoka, Japan) were used. Rats had free access to food and water, and were kept in uncrowded conditions (two/cage) in a light-, temperature-, and humidity-regulated room (light on 07.00–19.00, 23±3℃, and 50±20%).

Study design

T1 measurements in the brains of three normal rats and phantom studies were performed to identify pulse sequences, among which Gd-DTPA-induced signal enhancements in rat C6 brain gliomas were compared, and to determine pulse sequence parameters. Using the determined pulse sequences and parameters, we examined five rats with developed gliomas out of 20 rats that received C6 glioma implantation in their thalamus region.

MR imaging system

All scanning was performed on a 3T whole-body scanner (Signa LX VH3M4; GE Healthcare, Milwaukee, Wisc., USA) equipped with the manufacturer's gradient system (maximum gradient strength 40 mT/m; slew rate 150 mT/m/s).

For imaging rat brains, we built a three-turn solenoid coil with a diameter of 42 mm and a length along the cylindrical axis of 18 mm. The diameter and length of this coil were adjusted to rat head size. The helical pitch of the coil was wide enough to pass the ear bars used to secure the rat's head. The coil was capable of transmission and reception, and was tuned to an impedance of 50 Ω at a resonant frequency of 127.76 MHz. Capacitance was divided into six elements in series, which were put at each half turn. The coil was mounted on a fixing apparatus (Narishige Co., Ltd., Tokyo, Japan) using an acrylic jig specially designed for the coil (Fig. 1). Rats were placed prone on the fixing apparatus. Rat heads were secured using an incisor hook and ear bars. All components of the fixing apparatus consisted of non-magnetic materials. During imaging, the fixing apparatus, on which the rat and the coil were mounted, was placed in the gantry so that the cylindrical axis of the coil and the cranial-to-caudal direction of the rat were perpendicular to a static magnetic field, and the center of the rat brain was positioned at the magnet isocenter.

Measurement of T1 in normal rat brain

This measurement was performed to establish the normal T1 value in the transplantation site (thalamus) of the C6 glioma cells. T1 values in the brain of three normal rats (9–13 weeks old, 380±50 g) were

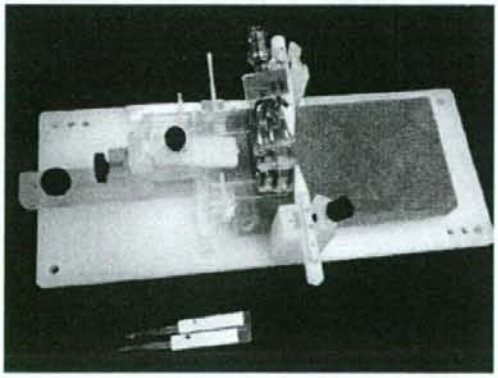

Fig. 1. The three-turn solenoid coil and the fixing apparatus used for the imaging of rats in the present study. The coil was mounted on the fixing apparatus using the specially designed acrylic jig.

Acta Radiologica rad134548.3d 23/10/07 20:33:23
The Charlesworth Group, Wakefield +44(0)1924 369598 - Rev 7.51n/W (Jan 20 2003)
262880

measured by using a saturation recovery method with a variable repetition time (TR) SE imaging sequence (16): TR 600, 1000, 2000, 4000, 8000 ms; echo time (TE) 10 ms; bandwidth (BW) 16 kHz; field of view (FOV) 40 × 30 mm; matrix size 256 × 160; slice thickness 1 mm; slice gap 1 mm; number of slices 16; number of excitations (NEX) 1; coronal plane. An 8-cm polyvinyl chloride tube with an outer diameter of 2.7 mm was inserted into the animal's trachea, and the rats were ventilated with an average of 2–3 ml per breath of a mixture of O_2, N_2, and air (2:1:10) using a small animal ventilator (CWE SAR-830/AP Ventilator; CWE, Inc., Ardmore, Pa., USA) at an average of 80 breaths per minute. Body temperature was monitored rectally (36.0 ± 0.5°C).

T1 values were estimated on a pixel-by-pixel basis using the non-linear least-square fit of the signal intensity measured for each TR value. In the obtained T1 images, regions of interest (ROIs) were placed on the thalamus, hippocampus, olfactory bulb, cerebral cortex, corpus callosum, midbrain, cerebellum, pons, cerebrospinal fluid, and muscle. Mean T1 values were calculated from each ROI. A mean and a standard deviation of the mean values obtained from three rats were calculated.

Phantom study

Phantom preparation. Gd-DTPA (Magnevist; Bayer Schering Pharma, Osaka, Japan) was diluted with saline to obtain 19 solutions with different concentrations (0, 0.01, 0.03, 0.05, 0.07, 0.1, 0.15, 0.2, 0.25, 0.3, 0.5, 0.7, 1, 3, 5, 7, 10, 30, and 50 mM). Each solution was encapsulated in separate polypropylene vials with a diameter of 27 mm, which were set in agar.

T1 measurement. T1 values of each Gd-DTPA solution were measured at room temperature using the same pulse sequence as the T1 measurement in normal rats: TR 34, 100, 200, 400, 600, 800, 1000, 1200, 1400, 1600, 1800, 2000, 4000, 6000, 8000, 11,000, 15,000 ms; TE 9 ms; BW 16 kHz; FOV 210 × 158 mm; matrix size 256 × 192; slice thickness 3 mm; number of slices 1; NEX 1. A standard quadrature birdcage head coil was used.

Circular ROIs with 70–80% of the diameter of a vial were placed on a homogeneous signal portion of each phantom image. T1 values were estimated by non-linear least-square fit of the average signal intensity of all voxels in the ROI measured for each TR value. Five measurements were performed for phantoms, and the mean and standard deviation of measured T1 values were calculated.

Choice of pulse sequences. We used a Gd-DTPA saline solution (0.1 mM) with a T1 value close to that in the normal thalamus as a corresponding solution to the glioma in the thalamus region before contrast. We hypothesized that T1 in the glioma would not be so different from that in normal tissue. Saline solutions with a higher concentration of Gd-DTPA were regarded as a corresponding solution to the glioma after contrast.

T1W images of each phantom were acquired at room temperature (approximately 21°C) using four clinically available pulse sequences (SE, fast SE [FSE], IR-FSE [T1FLAIR], and fast spoiled GRE [FSPGR]) (Table 1). A standard quadrature birdcage head coil was used for the imaging of phantoms.

Circular ROIs with 70–80% of the diameter of the vial were placed on a uniform signal portion of each phantom. Mean signal intensities were calculated from each ROI. For each sequence, signal enhancements of each Gd-DTPA solution (E_P) were calculated as $E_P = S/S_0$, where S is the signal intensity of each solution and S_0 is that of 0.1 mM of the solution. The pulse sequences showing high E_P were used for the imaging of C6 glioma model rats and were compared based on Gd-DTPA-induced signal enhancements in brain tumors, delineated by histopathology.

Rat brain C6 glioma model study

Preparation of rat brain C6 glioma models. C6 glioma cells (CCL-107 cell line, ATCC; Summit Pharmaceuticals International Corporation, Tokyo,

Table 1. Pulse sequences and imaging parameters used for imaging of saline phantoms containing gadopentetate dimeglumine (Gd-DTPA)

Pulse sequence	TR, ms	TE, ms	TI, ms	FA, °	ETL	BW, kHz	NEX	Acquisition time, min:s
SE	1400	14	—	—	—	16	1	4:46
FSE	1400	16	—	—	3	32	1	1:52
T1FLAIR	3000	16	1300	—	3	32	1	4:00
FSPGR	20	3.2	—	30	—	32	10	0:39

For all pulse sequences, FOV was 210 × 158 mm, matrix was 256 × 192, the number of slices was 1, and the slice thickness was 3 mm. SE: spin echo; FSE: fast spin echo; T1FLAIR: inversion recovery fast spin echo; FSPGR: fast spoiled gradient echo; TR: repetition time; TE: echo time; TI: inversion time; FA: flip angle; ETL: echo train length; BW: bandwidth; NEX: number of excitations.

Japan) were implanted into the region of the thalamus in the left hemispheres of the brains of 20 rats (8 weeks old, 292.8±14.8 g). The implantation procedures were performed under general anesthesia using an intramuscular injection of ketamine (33 mg/kg; Sankyo Co., Ltd., Tokyo, Japan) and xylazine (7 mg/kg; Bayer AG, Leverkusen, Germany). A burr hole was made 3 mm lateral and 2 mm posterior to the bregma using a dental drill. A needle with an outer diameter of 0.3 mm was inserted 4 mm below the outer table of the skull through the burr hole. A 10-μl solution containing 10^7 cells/ml was infused over 5 min at a constant rate using a microsyringe (Hamilton Co., Reno, Nev., USA) and infusion pump (Eicom Corp., Kyoto, Japan).

MR imaging. Two weeks after implantation, all 20 rats underwent screening by T1W imaging after Gd-DTPA administration. Developed glioma was confirmed in only five out of 20 rats. Those five rats were used for experiments for the comparison of pulse sequences. Three weeks after implantation, when the glioma was fully developed, T1W brain images of the selected five rats (11 weeks old, 301.3±29.0 g) were acquired before and after Gd-DTPA administration using three pulse sequences determined by the phantom study (Table 2) in the coronal plane. Rats were given general anesthesia with an intramuscular injection of a ketamine (33 mg/kg) and xylazine (7 mg/kg) mixture, and allowed to breathe spontaneously during preparation and imaging. First, precontrast T1W images were acquired. Then, a dose of 0.1 mmol/kg of Gd-DTPA was administered by hand injection followed by a 3.0-ml saline flush through a 22G indwelling needle placed in a tail or femoral vein. Postcontrast T1W imaging started 1 min after Gd-DTPA administration with identical settings to the precontrast imaging. Each rat was examined using all three pulse sequences (Table 2). In order to eliminate the effect of previously administered Gd-DTPA, three scans using different pulse sequences were performed on three separate days, at 22- to 26-hour intervals, in a randomized order.

ROI analysis. Based on the results of histopathology (see below), ROIs were placed on a portion of each glioma. Areas of necrosis or hemorrhage were excluded from the ROI. Mean signal intensities in the pre- and postcontrast T1W images were calculated from each ROI. For each sequence, signal enhancement of each glioma (E_T) was calculated as $E_T=S_{post}/S_{pre}$, where S_{post} is signal intensity in the glioma after contrast and S_{pre} is that before contrast.

Histopathology

One day after MR imaging, rat brains were removed and fixed in formalin. All brains were completely coronally sectioned. Sections were stained with hematoxylin and eosin (HE) in order to delineate areas of glioma, hemorrhage, and necrosis.

Statistical analysis

All parameters assessed were given as means ± standard deviations. Pair-wise comparison among pulse sequences was performed using the Tukey-Kramer test. A P value of <0.05 was considered statistically significant.

Results

T1 in normal rat brains

Fig. 2 shows images from one of the three normal rats used to quantitate T1 values in the brain. Table 3 summarizes the T1 values of typical brain structures. The T1 value in the thalamus was 1405±32 ms.

T1 of Gd-DTPA solutions

Fig. 3 shows selected images from a series of 17 images obtained with different TR values. Table 4 summarizes T1 values in the Gd-DTPA solutions

Table 2. Pulse sequences and imaging parameters used for imaging of rat brains with C6 glioma cell implants

Pulse sequence	TR, ms	TE, ms	FA, °	ETL	BW, kHz	NEX	Acquisition time, min:s
SE	1400	13	—	—	16	1	4:46
FSE	1400	18.6	—	3	32	3	4:32
FSPGR	20	4.7	30	—	32	8	5:40

For all pulse sequences, FOV was 60×45 mm, matrix was 256×192, the number of slices was 11, and the slice thickness was 2.5 mm (0.5-mm gap). SE: spin echo; FSE: fast spin echo; FSPGR: fast spoiled gradient echo; TR: repetition time; TE: echo time; FA: flip angle; ETL: echo train length; BW: bandwidth; NEX: number of excitations.

Acta Radiologica rad134548.3d 23/10/07 20:33:24
The Charlesworth Group, Wakefield +44(0)1924 369598 - Rev 7.51n/W (Jan 20 2003)
262880

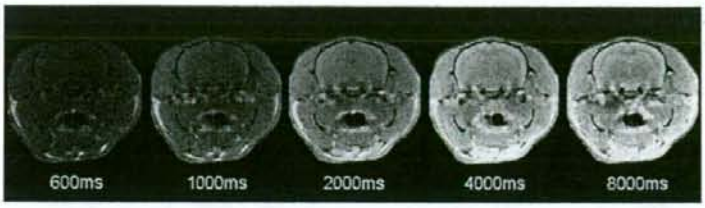

Fig. 2. Images from one of three rats used for the measurement of T1 values in normal rat brain. One of 16 slices acquired is shown. The images are arranged from left to right in ascending order of repetition time. All five images are set with equal window width and equal window level.

Table 3. T1 relaxation time in normal rat brain at 3T

	T1, ms
Thalamus	1405±32
Hippocampus	1779±151
Olfactory bulb	1613±117
Cerebral cortex	1506±13
Corpus callosum	1389±43
Midbrain	1329±50
Cerebellum	1726±356
Pons	1343±80
Cerebrospinal fluid	3460±737
Muscle	1529±99

Mean and standard deviation of values obtained from three rats.

ranging from 0 to 10 mM. In 30 and 50 mM solutions, an accurate T1 value could not be measured because of extensive signal loss due to T2 decay. The 0.1-mM solution showed a T1 value (1302±54 ms) closest to that in the normal thalamus (1405±32 ms).

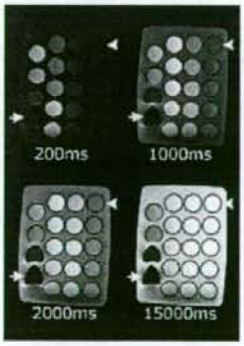

Fig. 3. Images obtained in the measurement of T1 values of 19 saline solutions with different concentrations of gadopentetate dimeglumine (0, 0.01, 0.03, 0.05, 0.07, 0.1, 0.15, 0.2, 0.25, 0.3, 0.5, 0.7, 1, 3, 5, 7, 10, 30, and 50 mM). The four selected images from a series of 17 images obtained with different TR values are shown. Each solution was encapsulated in separate polypropylene vials, which were set in agar. The concentration of gadopentetate dimeglumine decreases from bottom to top and from left to right. Arrows and arrowheads denote the 50-mM and 0-mM solutions, respectively. All four images are set with equal window width and equal window level.

Table 4. T1 of saline with different concentrations of Gd-DTPA at 3T

Gd-DTPA concentration, mM	T1, ms
0	3026±121
0.01	2652±96
0.03	2245±108
0.05	1970±92
0.07	1775±103
0.1	1302±54
0.15	993±57
0.2	820±52
0.25	737±51
0.3	666±63
0.5	389±17
0.7	284±12
1	209±9
3	84±4
5	58±2
7	36±1
10	27±1
30	—
50	—

Mean and standard deviation of values obtained from five measurements.

Choice of pulse sequences

Fig. 4 shows E_P in the Gd-DTPA solutions ranging from 0.1 to 50 mM. In Gd-DTPA solutions ranging from 0.15 to 30 mM, a higher E_P was obtained as follows: FSPGR > SE > FSE > T1FLAIR. Because E_P for T1FLAIR was lowest at all concentrations, T1FLAIR was not used for the imaging of rat brain tumors.

Based on our preliminary experiments, the T1 value in the glioma in the thalamus region after contrast was about 90% of that before contrast. Therefore, we regarded the 0.15-mM solution as a corresponding solution to glioma after contrast, and compared E_P values at 0.15 mM obtained using different sequences (Fig. 5). E_P at 0.15 mM was 1.10±0.02 for FSE, 1.16±0.01 for FSPGR, 1.16±0.01 for SE, and 1.06±0.01 for T1FLAIR. The Tukey-Kramer test showed significant differences ($P<0.05$) between all pairs except for FSPGR–SE. E_P for FSPGR was significantly higher than that for FSE and T1FLAIR and comparable to that for SE.

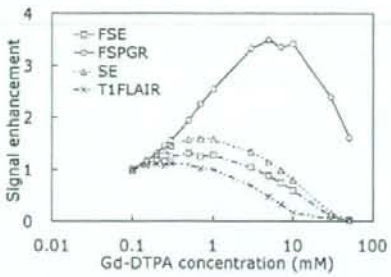

Fig. 4. Signal enhancements in saline solutions containing gadopentetate dimeglumine (Gd-DTPA) obtained by the following pulse sequences: spin echo (SE); fast spin echo (FSE); inversion recovery fast spin echo (T1FLAIR); fast spoiled gradient echo (FSPGR). Signal enhancement was the signal intensity scaled by that of a 0.1-mM Gd-DTPA solution whose T1 value was closest to the average T1 value in the brain parenchyma of normal rats.

Signal enhancement in rat brain C6 glioma

Fig. 6 displays typical pre- and postcontrast T1W images of brains of C6 glioma model rats, together with an example of ROIs placed on the glioma and HE-stained slices. Fig. 7 shows the comparison between E_T values for FSE, SE, and FSPGR. E_T values were 1.12 ± 0.05 for FSE, 1.26 ± 0.11 for FSPGR, and 1.20 ± 0.11 for SE. The Tukey-Kramer test showed the significant superiority of FSPGR over FSE. There was no significant difference between FSPGR and SE.

Discussion

T1W imaging using SE results in a corresponding restriction in the number of slices as a result of the

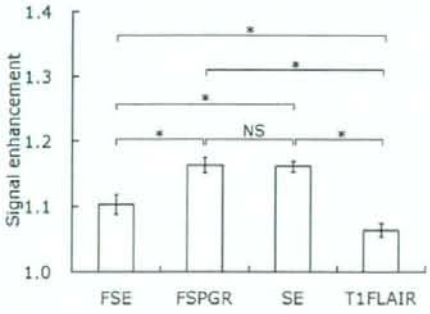

Fig. 5. Signal enhancement of saline solution with 0.15 mM Gd-DTPA obtained using different pulse sequences: spin echo (SE); fast spin echo (FSE); inversion recovery fast spin echo (T1FLAIR); fast spoiled gradient echo (FSPGR). Signal enhancement was defined as the signal intensity of a 0.15-mM solution scaled by that of a 0.1-mM solution. The Tukey-Kramer test was performed for pair-wise comparison among four pulse sequences. The asterisk and NS denote significant difference ($P<0.05$) and no significant difference ($P>0.05$), respectively.

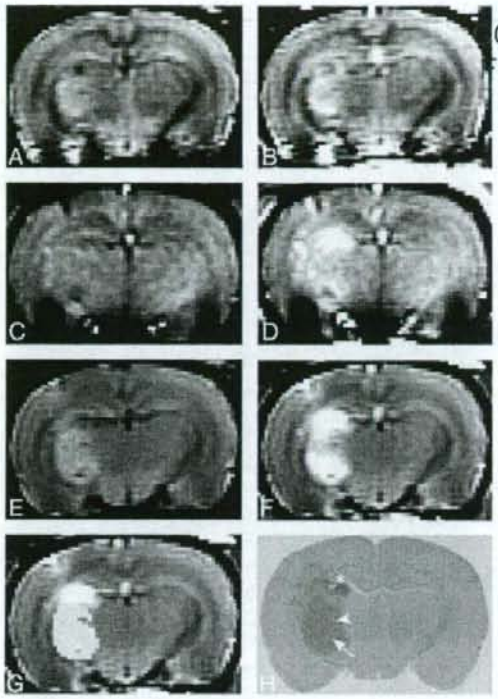

Fig. 6. Examples of pre- (A, C, E) and post-contrast (B, D, F) coronal T1-weighted images obtained using fast spin-echo (FSE) (A, B), fast spoiled gradient-echo (FSPGR) (C, D), and spin-echo (SE) (E, F) sequences. A region of interest (ROI) placed on the glioma (G) and a slice stained using hematoxylin and eosin (HE) (H). T1-weighted images were acquired 3 weeks after the implantation of C6 glioma cells. Areas of necrosis or hemorrhage, which were delineated based on histopathology, were excluded from ROIs. In the HE-stained slice, small-cell glioma (arrowhead), hemorrhage (asterisk), and necrosis (arrow) were found.

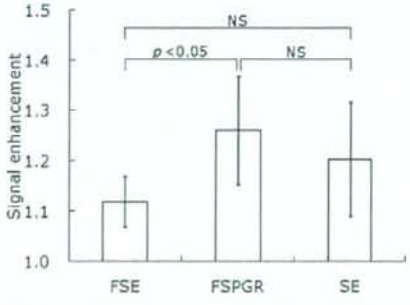

Fig. 7. Signal enhancement in rat brain C6 glioma obtained with different pulse sequences: spin echo (SE); fast spin echo (FSE); fast spoiled gradient echo (FSPGR). Signal enhancement was defined as the signal intensity after Gd-DTPA administration scaled by that before administration. The pair-wise comparison among pulse sequences was performed using the Tukey-Kramer test. NS denotes no significant difference ($P>0.05$).

specific absorption rate (SAR) at 3T. The use of FSE makes radiofrequency heating more serious. Compared to SE and FSE, FSPGR provides relatively low radiofrequency heating and, if the NEX of FSPGR can be reduced, relatively short acquisition time. This depends on the signal-to-noise ratio, and we thought it possible based on our rat brain images (Fig. 6). Therefore, we examined the characteristics of signal enhancement in FSPGR. FSPGR provided significantly higher signal enhancement than FSE and comparable signal enhancement to SE, both in the 0.15-mM Gd-DTPA solution and in rat brain C6 glioma in the thalamus region. We speculate that FSPGR may be superior to FSE and comparable to SE in its ability to delineate brain tumors, although, in order to verify this speculation, several studies would be required using different cell types and various transplantation sites. Considering the advantage of FSPGR in terms of acquisition time and SAR limit, FSPGR may be more suitable for contrast-enhanced T1W imaging of brain tumors in clinical 3T scanners than SE. Additionally, high-resolution 3D images can be obtained by using FSPGR with a reasonable acquisition time so that small lesions may be better visualized. On the other hand, FSPGR was more sensitive to magnetic susceptibility artifacts than SE (Fig. 6). SE could therefore be more suitable than FSPGR for delineation of tumors in regions with susceptibility artifacts, such as the base of the skull.

E_T values obtained in our study (1.26 for FSPGR, 1.20 for SE, and 1.12 for FSE) were lower compared to previously reported values (1, 4, 5, 12). For example, RUNGE et al. reported that the E_T induced by Gd-DTPA was approximately 1.44 using SE in rat brain C6/LacZ glioma models at 3T (5). The difference between E_T in our study and that in previous reports may result from the difference in the type of tumor, in the degree of growth of brain tumors, or in TR. In our study, TR was adjusted to increase T1 contrast in the normal brain region for specification of more exact location of the glioma. Although the use of a shorter TR may increase signal enhancement in the glioma, contrast in the normal region would become unclear, and therefore it could become difficult to specify the location of the glioma exactly. Therefore, we used a longer TR than that in previous reports.

FISCHBACH et al. showed higher contrast in SE in patients, but they optimized the TR (600 ms) of SE by phantom experiments using a saline solution with a low concentration of Gd-DTPA (0.125 μM) (12), whose T1 is extremely long compared to that in the brain. We quantified T1 in rat brains and chose a proper TR (1400 ms) of SE to enhance normal brain contrast. Therefore, our comparison would be fairer and our results may be more closely extrapolated to human tumors.

One limitation of our work is our limited sample size. Although C6 glioma cells were implanted into 20 rats in our in-vivo study, only five rats could be used for the experiment, as C6 gliomas showed considerable individual variation in their growth and were fully developed only in five rats. Therefore, the number of test animals was relatively small, resulting in large standard deviations for E_T. A larger sample size may show a significant difference between FSPGR and SE.

In conclusion, FSPGR is superior to FSE and comparable to SE in its ability to delineate rat brain C6 glioma in the thalamus region using venous injection of Gd-DTPA.

Acknowledgments

This study was supported by a research grant on Advanced Medical Technology from the Ministry of Health, Labor and Welfare (MHLW), Japan (H17-nano-15), and a Program for Promotion of Fundamental Studies in Health Science of the Organization for Pharmaceutical Safety and Research (of Japan) Health Science Research Grant (H13-005) from the Ministry of Health, Labor and Welfare, (of Japan)

References

1. Nöbauer-Huhmann IM, Ba-Ssalamah A, Mlynarik V, Barth M, Schoggl A, Heimberger K, et al. Magnetic resonance imaging contrast enhancement of brain tumors at 3 tesla versus 1.5 tesla. Invest Radiol 2002;37:114–9.
2. Trattnig S, Ba-Ssalamah A, Noebauer-Huhmann IM, Barth M, Wolfsberger S, Pinker K, et al. MR contrast agent at high-field MRI (3 Tesla). Top Magn Reson Imaging 2003;14:365–75.
3. Ba-Ssalamah A, Nöbauer-Huhmann IM, Pinker K, Schibany N, Prokesch R, Mehrain S, et al. Effect of contrast dose and field strength in the magnetic resonance detection of brain metastases. Invest Radiol 2003;38:415–22.
4. Biswas J, Nelson CB, Runge VM, Wintersperger BJ, Baumann SS, Jackson CB, et al. Brain tumor enhancement in magnetic resonance imaging: comparison of signal-to-noise ratio (SNR) and contrast-to-noise ratio (CNR) at 1.5 versus 3 tesla. Invest Radiol 2005;40: 792–7.
5. Runge VM, Biswas J, Wintersperger BJ, Baumann SS, Jackson CB, Herborn CU, et al. The efficacy of gadobenate dimeglumine (Gd-BOPTA) at 3 Tesla in brain magnetic resonance imaging: comparison to 1.5

Tesla and a standard gadolinium chelate using a rat brain tumor model. Invest Radiol 2006;41:244–8.
6. Chappell PM, Pelc NJ, Foo TK, Glover GH, Haros SP, Enzmann DR. Comparison of lesion enhancement on spin-echo and gradient-echo images. Am J Neuroradiol 1994;15:37–44.
7. Rand S, Maravilla KR, Schmiedl U. Lesion enhancement in radio-frequency spoiled gradient-echo imaging: theory, experimental evaluation, and clinical implications. Am J Neuroradiol 1994;15:27–35.
8. Pui MH, Fok EC. MR imaging of the brain: comparison of gradient-echo and spin-echo pulse sequences. Am J Roentgenol 1995;165:959–62.
9. Fellner F, Holl K, Held P, Fellner C, Schmitt R, Bohm-Jurkovic H. A T1-weighted rapid three-dimensional gradient-echo technique (MP-RAGE) in preoperative MRI of intracranial tumours. Neuroradiology 1996;38: 199–206.
10. Li D, Haacke EM, Tarr RW, Venkatesan R, Lin W, Wielopolski P. Magnetic resonance imaging of the brain with gadopentetate dimeglumine-DTPA: comparison of T1-weighted spin-echo and 3D gradient-echo sequences. J Magn Reson Imaging 1996;6:415–24.
11. Elster AD. How much contrast is enough? Dependence of enhancement on field strength and MR pulse sequence. Eur Radiol 1997;7 Suppl 5:276–80.
12. Fischbach F, Bruhn H, Pech M, Neumann F, Ricke J, Felix R, et al. Efficacy of contrast medium use for neuroimaging at 3.0 T: utility of IR-FSE compared to other T1-weighted pulse sequences. J Comput Assist Tomogr 2005;29:499–505.
13. Raila FA, Bowles AP Jr, Perkins E, Terrell A. Sequential imaging and volumetric analysis of an intracerebral C6 glioma by means of a clinical MRI system. J Neurooncol 1999;43:11–7.
14. Thorsen F, Ersland L, Nordli H, Enger PO, Huszthy PC, Lundervold A, et al. Imaging of experimental rat gliomas using a clinical MR scanner. J Neurooncol 2003;63:225–31.
15. Blanchard J, Mathieu D, Patenaude Y, Fortin D. MR-pathological comparison in F98-Fischer glioma model using a human gantry. Can J Neurol Sci 2006;33: 86–91.
16. Wansapura JP, Holland SK, Dunn RS, Ball WS Jr. NMR relaxation times in the human brain at 3.0 tesla. J Magn Reson Imaging 1999;9:531–8.

Acta Radiologica rad134548.3d 23/10/07 20:33:45
The Charlesworth Group, Wakefield +44(0)1924 369598 - Rev 7.51n/W (Jan 20 2003)

262880

Ann Nucl Med (2008) 22:667–675
DOI 10.1007/s12149-008-0157-9

ORIGINAL ARTICLE

Optimal scan time of oxygen-15-labeled gas inhalation autoradiographic method for measurement of cerebral oxygen extraction fraction and cerebral oxygen metabolic rate

Miho Shidahara · Hiroshi Watabe · Kyeong Min Kim
Nobuyuki Kudomi · Hiroshi Ito · Hidehiro Iida

Received: 7 March 2008 / Accepted: 1 May 2008

Abstract
Objective Regional cerebral blood flow (CBF), cerebral blood volume, oxygen extraction fraction (OEF), and cerebral metabolic rate of oxygen ($CMRO_2$) can be estimated from $C^{15}O$, $H_2{}^{15}O$, and $^{15}O_2$ tracers and positron emission tomography (PET) using an autoradiographic (ARG) method. Our objective in this study was to optimize the scan time for $^{15}O_2$ gas study for accurate estimation of OEF and $CMRO_2$.
Methods We evaluated statistical noise in OEF by varying the scan time and error caused by the tissue heterogeneity in estimated OEF and $CMRO_2$ using computer simulations. The characteristics of statistical noise were investigated by signal-to-noise (S/N) ratio from repeated tissue time activity curves with noise, which were generated using measured averaged arterial input function and assuming CBF = 20, 50, and 80 (ml/100 g per minute). Error caused by tissue heterogeneity was also investigated by estimated OEF and $CMRO_2$ from tissue time activity curve with mixture of gray and white matter varying fraction of mixture. In the simulations, three conditions were assumed (i) CBF in gray and white matter (CBF^g and CBF^w) was 80 and 20, OEF in gray and white matter (E^g and E^w) was 0.4 and 0.3, (ii) CBF^g and CBF^w decreased by 50%, and E^g and E^w increased by 50% when compared with conditions (i) and (iii). CBF^g and CBF^w decreased by 80%, and E^g and E^w increased by 50% when compared with condition (i).
Results The longer scan time produced the better S/N ratio of estimated OEF value from three CBF values (20, 50, and 80). Errors of estimated OEF for three conditions owing to tissue heterogeneity decreased, as scan time took longer. Meanwhile in the case of $CMRO_2$, 3 min of scan time was desirable.
Conclusions The optimal scan time of $^{15}O_2$ inhalation study with the ARG method was concluded to be 3 min from taking into account for maintaining the S/N ratio and the quantification of accurate OEF and $CMRO_2$.

Keywords O-15 oxygen gas · Positron emission tomography · Autoradiographic method

M. Shidahara (✉) · H. Ito
Molecular Imaging Center, National Institute of Radiological Sciences, 4-9-1 Anagawa, Inage-ku, Chiba 263-8555, Japan
e-mail: sidahara@nirs.go.jp

H. Watabe · K.M. Kim · N. Kudomi · H. Iida
Department of Investigative Radiology, National Cardiovascular Center Research Institute, Osaka, Japan

Introduction

Quantitative cerebral oxygen extraction fraction (OEF) and cerebral metabolic rate of oxygen ($CMRO_2$) images can be measured by oxygen-15-labeled gas ($^{15}O_2$) and positron emission tomography (PET). These physiological parameters have provided important hemodynamic information for the diagnoses of cerebrovascular disease, especially in the case of misery perfusion [1–3]. For effective application of these parameters to urgent clinical study, a simplified diagnostic method to shorten scan time is strongly required and yet retaining the quantification. When compared with the steady-state method, the autoradiographic (ARG) method [4] has the potential to shorten the length of study [5]. A 3-min scan duration following $^{15}O_2$ inhalation has been used by Hatazawa et al. [6]; however, earlier no systematic investigation of optimization of scan time for $^{15}O_2$ study with the ARG method was performed. In this article, by focusing on two factors, namely, signal-to-noise (S/N) ratio on the

functional images and the tissue heterogeneity, the optimal scan duration for the ARG method with $^{15}O_2$ gas was investigated.

Variance of pixel counts in reconstructed image is delivered from randomly emitted and detected photon counts and then propagates to estimated OEF and $CMRO_2$ value. The short physical half-life (about 2 min) of ^{15}O causes large variance of the pixel counts, and, therefore, alternation of the scan duration leads to substantial change on the image quality of PET image, such as S/N ratio.

The influence of tissue heterogeneity on estimated physiological parameters has been reported by several authors [7, 8], and estimation error of cerebral blood flow (CBF) is caused by the assumption that there is only single-tissue CBF in mixed region of gray and white matter, even though different tissues own different CBF values. An optimization scheme of measurement of CBF was provided by Kanno et al. [7, 9], and that study showed the error of estimated CBF from tissue heterogeneity depended on scan time [9]. The effect of tissue heterogeneity in systematic error of OEF has been also analyzed for the steady-state method [10, 11]. However, in the case of the estimation of OEF and $CMRO_2$ with the ARG method and bolus inhalation of $^{15}O_2$, the effects of tissue heterogeneity in $^{15}O_2$ study and the effect of the error in CBF owing to tissue heterogeneity propagates to OEF and $CMRO_2$ estimates are unknown.

In this article, we performed computer simulations of the ARG method with ^{15}O water and $^{15}O_2$ gas under three clinical conditions, namely, normal, misery perfusion, and occlusion. We investigated the relationship between scan time and S/N ratio of estimated OEF. Furthermore, the relationship between scan time and the accuracy in estimated OEF and $CMRO_2$ affected by tissue heterogeneity for both ^{15}O water and $^{15}O_2$ gas studies was examined. By these results, optimized scan time for $^{15}O_2$ gas inhalation protocol was determined especially for clinical application such as ischemic disease.

Materials and methods

Computing CBF, OEF, and $CMRO_2$ using the ARG method

In the ARG method, CBF (ml/g per minute) is computed by a single-tissue compartment model described as follows:

$$\int_0^T C_t^{W}(t)\mathrm{d}t = \rho_b \int_0^T \mathrm{CBF}\cdot A(t)\otimes \mathrm{e}^{-\rho_b \frac{\mathrm{CBF}}{p}}\,\mathrm{d}t \qquad (1)$$

where $C_t^{W}(t)$ (cps/ml) is the radioactivity concentration of $H_2{}^{15}O$ study at time t measured by PET (integrated from time 0 to time T), ρ_b is the density of brain tissue (1.04) (g/ml), $A(t)$ (cps/ml) is arterial input function of $H_2{}^{15}O$ at time t measured by the external radiation detector, and p is the partition coefficient factor (fixed as 0.8 ml/ml) [12]. The CBF value for each pixel is estimated in the look-up table manner with observer PET data $\int_0^T C_t^{W}(t)\mathrm{d}t$ against $\rho_b \int_0^T \mathrm{CBF}\cdot A(t)\otimes \mathrm{e}^{-\rho_b \frac{\mathrm{CBF}}{p}}\,\mathrm{d}t$.

Using the ARG method, OEF and $CMRO_2$ are computed owing to a model by Mintun et al. [4] described as follows:

$$\begin{aligned}\int_0^T C_t^{O}(t)\mathrm{d}t = \rho_b \int_0^T & \mathrm{CBF}\cdot A_{H_2O}(t)\otimes \mathrm{e}^{-\rho_b \frac{\mathrm{CBF}}{p}} \\ & + \mathrm{OEF}\cdot \mathrm{CBF}\cdot A_{O_2}(t)\otimes \mathrm{e}^{-\rho_b \frac{\mathrm{CBF}}{p}t} \\ & + \mathrm{CBV}\cdot \mathrm{VR}\cdot(1-\mathrm{OEF}\cdot \mathrm{FV})\cdot A_{O_2}(t)\mathrm{d}t \end{aligned} \qquad (2)$$

where $C_t^{O}(t)$ (cps/ml) is the radioactivity concentration of $^{15}O_2$ study at time t measured by PET (integrated from time 0 to time T), CBF (ml/g per minute) values are obtained from $H_2{}^{15}O$ study using Eq. 1, $A_{H_2O}(t)$ (cps/ml) and $A_{O_2}(t)$ (cps/ml) are the arterial input functions for $H_2{}^{15}O$ and $^{15}O_2$ components at time t measured by the external radiation detector. CBV is the cerebral blood volume and calculated by the additional PET scan with $C^{15}O$. VR is the small- to large-vessel hematocrit ratio (fixed as 0.85), FV is the effective venous fraction (fixed as 0.835) [4]. OEF is computed from the arterial input functions of $A_{H_2O}(t)$ and $A_{O_2}(t)$ and fixed values for p, VR and FV by the look-up table manner in the pixel-by-pixel basis. $CMRO_2$ is then calculated as follows:

$$\mathrm{CMRO_2} = \mathrm{CBF}\cdot \mathrm{OEF}\cdot [\mathrm{O_2}]_a \qquad (3)$$

where $[O_2]_a$ is the arterial oxygen concentration which is given as follows:

$$[\mathrm{O_2}]_a = 1.39\cdot \mathrm{Hb}\cdot \%\mathrm{Sat} \qquad (4)$$

where 1.39 is the averaged oxygen volume associated with a single hemoglobin molecule, Hb is the hemoglobin concentration (g hemoglobin/ml blood), and %Sat is the percentage of saturation in O_2 of the arterial blood.

PET study

To compute CBF, OEF, and $CMRO_2$ images, three PET scans with $C^{15}O$ gas, ^{15}O water, and $^{15}O_2$ gas are required with additional transmission scan. The typical clinical

protocol in National Cardiovascular Center Hospital is as follows:

1. Ten-minute transmission scan with ^{68}Ge–^{68}Ga source.
2. The subject was made to inhale $C^{15}O$ (2.19 MBq per minute) for 1 min and 4 min after the start of the inhalation; PET scan is started for 4 min.
3. The subject is intravenously (right bronchial vein) administered $H_2^{15}O$ (0.81 MBq for 20 s bolus injection). PET scan (12 × 5 s, 2 × 15 s total 1.5 min) is started 10 s later from the start of infusion of $H_2^{15}O$.
4. The subject was made to inhale $^{15}O_2$ gas (2.19 MBq/min) for 1 min. PET scan (12 × 5 s, 8 × 15 s total 3 min) is started at the same time of the inhalation.

Positron emission tomography scanner is ECAT EXACT 47 (CTI, Knoxville, TN, USA), and all scans are performed with 2D mode (septa extended). For the present study, scan protocol of $^{15}O_2$ gas was extended from conventional 180 s to 300 s (12 × 5 s, 8 × 15 s, and 4 × 30 s).

For the simulations studies, arterial input functions of $A_{H_2O}(t)$ and $A_{O_2}(t)$ in Eq. 2 were mimicked from averaged whole-blood arterial input function of five healthy volunteers (all subjects were men, and mean age was 24.7 ± 3.6 years) [13]. Delay- and dispersion-corrected arterial input functions of the five subjects were averaged and separated into two-component, oxygen-gas, and metabolized water by convolution formula [14] (Fig. 1).

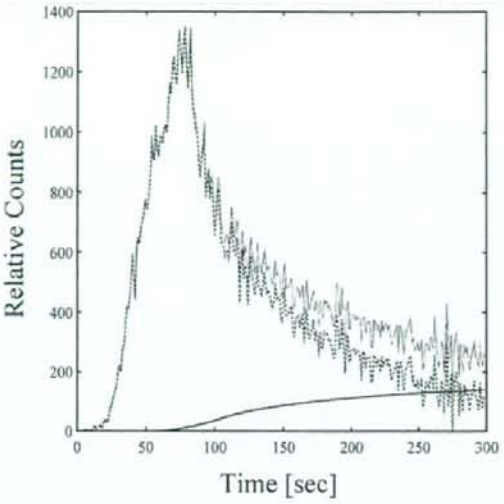

Fig. 1 Delay- and dispersion-corrected arterial input function: whole-blood curve [function: whole-blood curve (*solid line*), O_2 components (*dotted line*), and metabolized water components (*bold solid line*)]

Simulation studies

Two simulation studies were performed.

Simulation 1: S/N ratio in quantitative OEF images

The relationship between the scan duration and statistical noise of OEF values was investigated in terms of S/N ratio. The variance of PET data C_{PET} at frame i was estimated using the following equation [15, 16]:

$$\frac{\sigma(i)}{C_{PET}(i)} = \frac{c}{\sqrt{NEC(i)}} \tag{5}$$

where $\sigma(i)$ is standard deviation (SD) of C_{PET} at frame i and $NEC(i)$ is noise equivalent count [17] at frame i. c is constant factor. To determine c, phantom experiments were performed. A cylindrical phantom (16 cm in diameter and an axial length of 20 cm) filled with water was used for the measurement of statistical noise on reconstructed image. ^{15}O water solution (half-life is 2.04 min, 518 MBq at scan start) was injected in the phantom. Single-PET scanning with dynamic acquisition was performed to obtain 20 frames, each with duration of 60 s. Count rates of true coincidents and random coincidents detected by PET gantry were also recorded, and NEC for each frame was computed. Image reconstruction was performed by direct Fourier transform algorithm with 6.0 mm full width half maximum Gaussian filter that is used for the clinical routine. From each frame data, mean $C_{PET}(i)$ with $\sigma(i)$ were computed from all pixels inside the drawn circular ROI (10 cm in diameter) on the reconstructed image. The constant c was estimated by these data to fit Eq. 5.

To simulate the S/N ratio in the clinical PET study, $NEC(i)$ during PET acquisition was measured in actual PET studies with $^{15}O_2$ gas for five normal volunteers described in earlier section and the averaged $NEC(i)$ data were used in the simulation; 500 noisy simulated PET data, $C^j_{PET}(i)$ ($j = 1, \ldots, 500$) were generated according to Eqs. 2 and 5 under the conditions of CBF = 20, 50, and 80 (ml/100 g per minute) and OEF = 0.2, 0.4, and 0.8. The integration time T in Eq. 2 was set to 60 s, 120 s, 180 s, 240 s, and 300 s and at each integration time T, $OEF^j(T)$ was estimated from each $\int_0^T C^j_{PET}(i)di$ using the ARG method. The S/N ratios at time T were derived from the division of mean estimated $OEF(T)$ using 500 data sets by its SD.

Table 1 Predefined parameters for simulations of tissue heterogeneity

Condition	CBF^g (ml/100 g per minute)	CBF^w (ml/100 g per minute)	OEF^g	OEF^w
(i) Normal	80	20	0.4	0.3
(ii) Misery perfusion	40	10	0.6	0.45
(iii) Occlusion	16	4	0.6	0.45

Three conditions of (i) normal, (ii) misery perfusion, and (iii) occlusion were considered. Cerebral blood flow (CBF) in gray matter (CBF^g) and white matter (CBF^w), and oxygen extraction fraction (OEF) in gray matter (OEF^g) and white matter (OEF^w) were defined

Simulation 2: Tissue heterogeneity

The time dependency of quantitative error in estimated OEF and $CMRO_2$ caused by tissue heterogeneity was evaluated. We assumed that tissue TAC $C_t^m(t)$ in a mixed region of gray and white matter is expressed as

$$C_t^m(t) = \alpha \cdot C_t^g(t) + (1 - \alpha) \cdot C_t^w(t) \quad (6)$$

where α is the fraction of gray matter volume ranged from 0 to 1, and $C_t^g(t)$ and $C_t^w(t)$ are calculated tissue TACs in gray and white matter from Eqs. 1 and 2 with fixed parameters, respectively. In view of the clinical application for ischemic disease, three physiological conditions of (i) normal, (ii) misery perfusion, and (iii) occlusion were considered in the present simulations. CBF in gray matter and white matter, and OEF in gray matter and white matter were defined as shown in Table 1. CBF^m, OEF^m, and $CMRO_2^m$, including the effect of tissue heterogeneity was estimated by the ARG method with the integration time T of 90 s in $H_2{}^{15}O$ study and T = 120 s, 180 s, 240 s, and 300 s in $^{15}O_2$ study.

The magnitude of error in estimated CBF^m value at fixed scanning time of 90 s

Varying the fraction of gray volume [0:1], CBF^m of three conditions in (i), (ii), and (iii) was estimated by the ARG method and the differences between CBF^m and ideal CBF value CBF_{ave} in Eq. 7 were compared.

$$CBF_{ave} = \alpha \cdot CBF_g + (1 - \alpha) \cdot CBF_w \quad (7)$$

Time dependency of estimated OEF^m from CBF^m

For three conditions, $OEF^m(T)$ and $CMRO_2^m(T)$ at integration time T (= 120 s, 180 s, 240 s, and 300 s) were estimated using CBF^m value and the ARG method. Varying the fraction of gray volume [0:1] for $H_2{}^{15}O$ and $^{15}O_2$ study, OEF^m and $CMRO_2^m$ were compared with ideal OEF and $CMRO_2$ values (OEF_{ave} and $CMRO_{2ave}$), shown in Eq. 8:

$$OEF_{ave} = \alpha \cdot OEF^g + (1 - \alpha) \cdot OEF^w$$
$$CMRO_{2ave} = \alpha \cdot CMRO_2^g + (1 - \alpha) \cdot CMRO_2^w \quad (8)$$

In the calculations of $CMRO_2^m$, CBF^m values were employed.

Results

Simulation 1: S/N ratio in quantitative OEF images

Figure 2a shows the relationship between NEC and coefficient of variance (COV) which is defined as the ratio between SD of C_{PET} and C_{PET}. Constant factor c in Eq. 5 was estimated from the relationship using the least-squares fitting and resulted in 38.1 (r = 0.996). Figure 2b shows averaged NEC curve of 5 $^{15}O_2$ studies.

Oxygen extraction fraction under the condition of CBF = 20, 50, and 80 (ml/100 g per minute) was estimated using noise-added time activity curve (Fig. 3a) using calculated $\sigma(i)$ in Eq. 5 and averaged NEC curve. Figure 3 shows the relationship between integrated time T and S/N ratio in estimated OEF values [OEF = 0.4 (Fig. 3b), OEF = 0.2 (Fig. 3c), and OEF = 0.6 (Fig. 3d)]. In general, the longer scan time provided better S/N ratio as shown in Fig. 3. In the case of low OEF (i.e., OEF = 0.2), S/N ratio reached plateau more rapidly than other cases.

Actual OEF and $CMRO_2$ images computed by the ARG method with T = 60 s, 180 s for a young normal volunteer were shown in Fig. 4. Less statistical noise in both OEF and $CMRO_2$ images with T = 180 s was visually observed when compared with T = 60 s. This figure supports the simulation results.

Simulation 2: Tissue heterogeneity

The relationship between the error of estimated CBF^m for $H_2{}^{15}O$ study and the fraction of gray volume is shown in Fig. 5. Lower CBF values in both gray and white matters [i.e., condition (ii) CBF^g = 40, CBF^w = 10, or condition (iii) CBF^g = 16, CBF^w = 4] reduce the error of

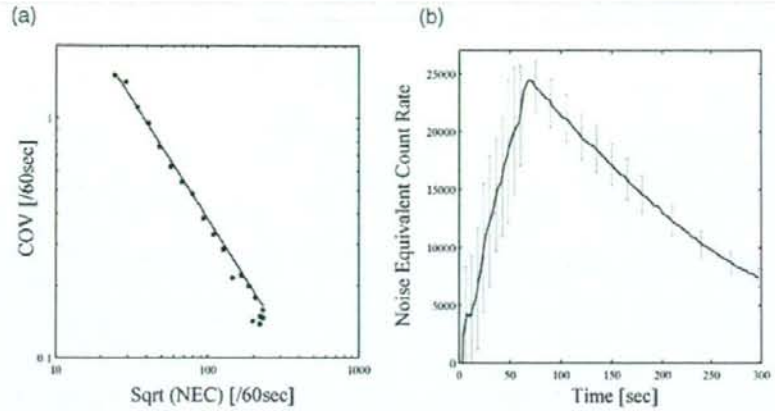

Fig. 2 a The relationship between noise equivalent count (NEC) and coefficient of variance (COV) obtained from phantom experiment with ECAT EXACT. b Averaged dynamic NEC curve with standard deviation of $^{15}O_2$ study among five volunteers

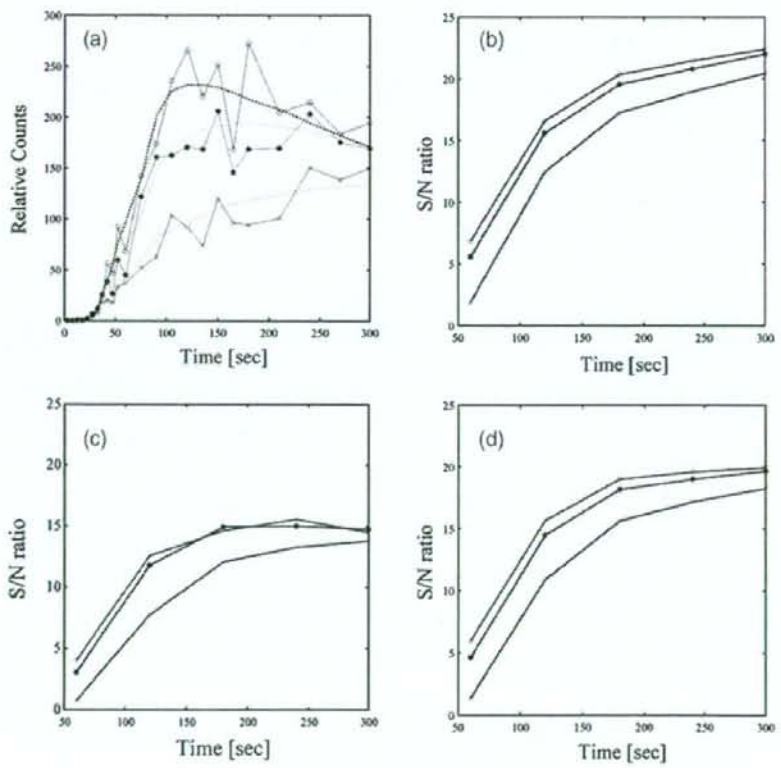

Fig. 3 a Noise-added time activity curves of $^{15}O_2$ study assuming oxygen extraction fraction (OEF) = 0.4 and cerebral blood flow (CBF) = 80 (*open circle*), 50 (*closed circle*), and 20 (*cross*; ml/100 g per minute), and true time activity curves (*dotted lines*). Time dependency of signal-to-noise ratio in estimated (b) OEF = 0.4, (c) OEF = 0.2, and (d) OEF = 0.6 using CBF = 80 (*open circle*), 50 (*closed circle*), and 20 (*cross*; ml/100 g per minute)

estimated CBF^m when compared with condition (i) $CBF^g = 80$, $CBF^w = 20$. The maximum error of CBF^m with three conditions of (i) normal, (ii) misery perfusion, and (iii) occlusion were −12.5% ($\alpha = 0.39$), −6.7% ($\alpha = 0.38$), and −2.8% ($\alpha = 0.35$), respectively.

Figures 6 and 7 show the relationship between the error of estimated $OEF^m(T)$ (a) and $CMRO_2^m(T)$ (b) and the relationship between the maximum error and scanning time. As shown in Fig. 7a, b, by increasing integration time, the error of estimated OEF^m and

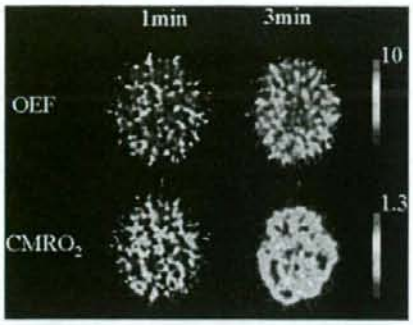

Fig. 4 An example of clinical images of OEF and cerebral metabolic rate of oxygen ($CMRO_2$) obtained from $T = 60$ s and 180 s scan time for a patient. Image reconstruction was performed with direct Fourier transform algorithm with 6 mm Gaussian filter. Reconstructed image has 128 × 128 × 47 slices with 1.84 mm × 1.84 mm and 3.38 mm pixel sizes. Attenuation correction using transmission data and scatter correction with the deconvolution scatter function were applied

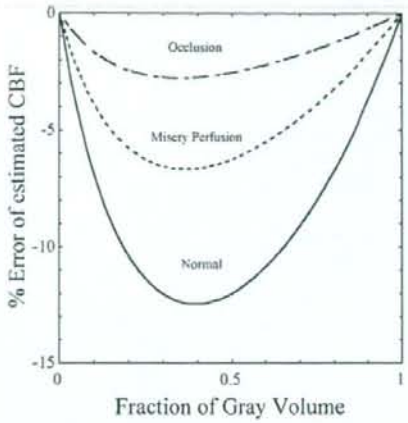

Fig. 5 The effect of tissue heterogeneity on % error of CBF^m in $CBF^s = 80$, $CBF^w = 20$ (*solid line*), $CBF^s = 50$, $CBF^w = 12$ (*dotted line*), and $CBF^s = 16$, $CBF^w = 4$ (*dotted dashed line*)

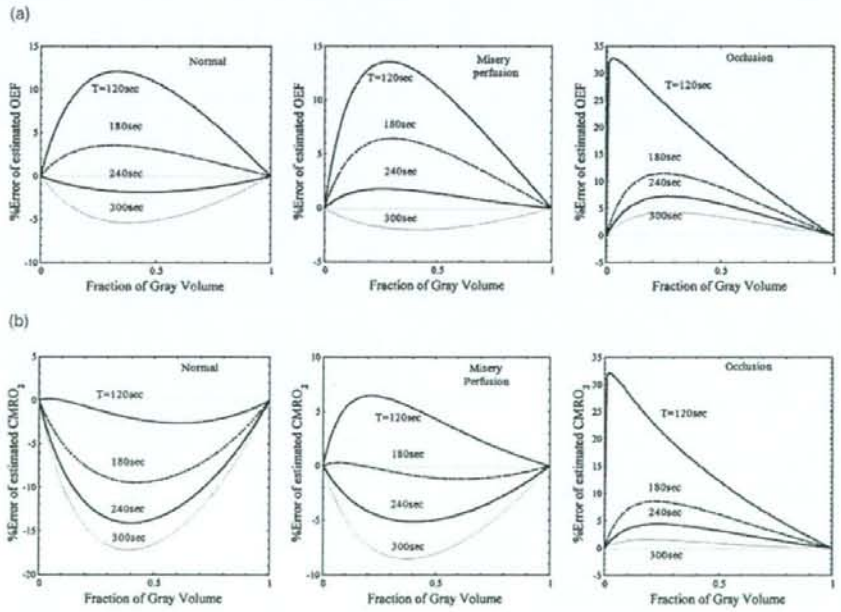

Fig. 6 The effect of tissue heterogeneity on % error of $OEF^m(T)$ (**a**) and $CMRO_2^m(T)$ (**b**) in normal, misery perfusion, and occlusion conditions for integration times of 120 s, 180 s, 240 s, and 300 s including the effect of tissue heterogeneity in $H_2{}^{15}O$ study

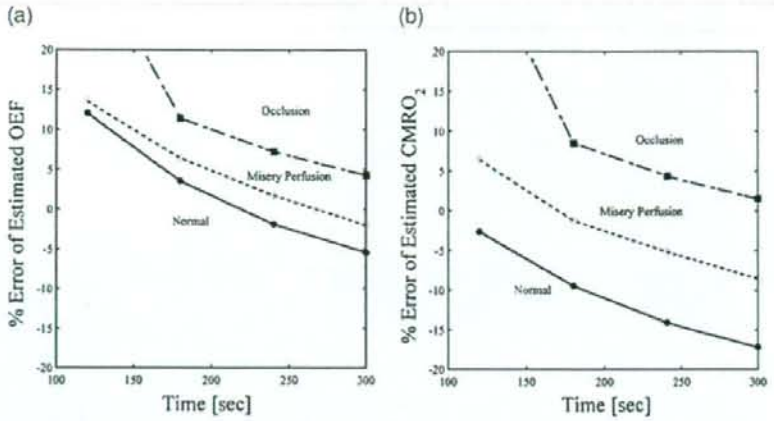

Fig. 7 The maximum error of estimated OEF^m (T) (**a**) and $CMRO_2^m$ (T) (**b**) for integration times of 120 s, 180 s, 240 s, and 300 s including the effect of tissue heterogeneity in $H_2{}^{15}O$ study. *Solid lines* are for normal conditions. *Dotted lines* are for misery perfusion conditions. *Dotted dashed lines* are for occlusion conditions

$CMRO_2^m$ tended to become negative values. In detail, for occlusion condition (iii) longer integration time provided smaller error of estimated OEF^m and $CMRO_2^m$. In misery perfusion condition (ii), the error of estimated OEF^m also became smaller error until 300 s, and then the error tended to become negative. The error of estimated $CMRO_2^m$ for condition (ii) is minimized to −1.22% at 180 s accumulation time. In normal condition (i), the error of estimated OEF^m was minimized to −1.9% at 240 s, and the error of estimated $CMRO_2^m$ was minimized to −2.63% at 120 s.

Discussion

In this study, for proper scan protocol of the ARG method in $^{15}O_2$ study, we simulated time dependency of accuracy and variation in physiological parameters with statistical noise and effect of tissue heterogeneity.

S/N ratio in estimated OEF

Variance of pixel counts in reconstructed images is delivered from randomly emitted and detected photon counts and then propagates to estimated OEF and $CMRO_2$ values. Actually, the statistical model of variance of pixel counts does not simply obey the Poisson statistics owing to several data processing (normalization, attenuation, and scatter corrections), which destroy the statistical relationship between expected and observed values. Earlier, there were investigations on developing the statistical model of pixel value [7, 15, 16]. Carson et al. [15] and Watabe et al. [16] modeled statistical variation of pixel value using NEC and then evaluated the adaptability of the model by the phantom and clinical studies. Their approach is simple and accurate enough, and so, we utilized their approach to simulate the noise.

We simulated the TAC $C_i(t)$ from lower to higher count level using three cases of CBF = 20, 50, and 80 (ml/100 g per minute) under three conditions of OEF values (0.2, 0.4, and 0.6), because the variation in OEF depends on the TAC counts level. As shown in Fig. 3, the longer scan time provides better S/N ratio. This figure indicates that the S/N ratio with low OEF and high CBF (Fig. 3c) reaches a plateau earlier than other cases. This is because that later points of TAC with low OEF and high CBF have little impact on the noise of estimates. Because $CMRO_2$ is the product with OEF and CBF, the characteristic of statistical noise of estimated $CMRO_2$ could be propagated from estimated OEF as well as estimated CBF values. Therefore, the maximum S/N ratio of the estimated $CMRO_2$ expects to show the same tendency as the S/N ratio of the estimated OEF if the statistical noise of the CBF was fixed.

In the present study, we assumed the noise-free arterial input function for the simulation. Furthermore, we added noise to arterial input function, but the tendency did not change (data are not shown).

Tissue heterogeneity

We showed that in the mixed region of gray and white matter, the non-linear relationship between physiological parameters and PET counts results in over-/underestimation of the physiological parameters. Figure 5 shows that a lower CBF such as ischemic disease leads to a small error of estimated CBF^m when compared with normal CBF because that effect of the non-linear relationship is less dominant than in the case of a high CBF value. This is consistent with results that Ito et al. [8]

showed high CBF value is more suffered from the tissue heterogeneity when compared with that low CBF value in SPECT study [8]. For the ARG PET study with $H_2{}^{15}O$ study, earlier research by Kanno et al. showed about 13% underestimation in estimated CBF owing to tissue heterogeneity for scan time, 120 s, assuming $CBF^{\sharp} = 80$, $CBF^{*} = 20$, $P = 1.0$, and gray matter fraction = 0.5 [9]. Even though there were slight differences in partition coefficient and scan time between Kanno et al. [9] and our study, underestimation in estimated CBF was about 12% for scan time 90 s, assuming $CBF^{\sharp} = 80$, $CBF^{*} = 20$, $P = 0.9$, and gray matter fraction = 0.5, which was almost similar results to Kanno et al. [9].

The errors of estimated OEF^{m} and $CMRO_2{}^{m}$ are propagated from such error of estimated CBF^{m}. As shown in Fig. 7, the results of the present study suggest that error of estimated physiological parameters with tissue heterogeneity will variously change positive or negative under the conditions (i), (ii), and (iii) with various scan times. The shorter scan time, the more overestimation was observed for OEF^{m} under the conditions (i), (ii), and (iii), and $CMRO_2{}^{m}$ especially under the condition (iii). This may be caused from the underestimation of CBF^{m}, which can be assumed to be the lower oxygen-15 oxy-hemoglobin supplement than true oxygen-15 oxy-hemoglobin supplement (= observed or simulated PET counts) especially at the early scan time, when the metabolized water component can be neglected. In the longer scan time, the more underestimation was observed for OEF^{m} under the conditions (i) and (ii) and $CMRO_2{}^{m}$ especially under the condition (i). There are earlier studies on tissue heterogeneity in estimated OEF for the steady-state method [10, 11]. Without considering error in estimated CBF, Lammertsma and Jones [10] showed that OEF values for every condition were underestimated owing to tissue heterogeneity. Correia et al. [11] investigated the effect of tissue heterogeneity on OEF considering the error in estimated CBF under the condition of the steady state. According to their studies, a small $OEF^{\sharp}$ value (i.e., $OEF^{\sharp} = 0.2$, $OEF^{*} = 0.4$) leads to overestimation in OEF, and a large $OEF^{\sharp}$ value ($OEF^{\sharp} = 0.8$, $OEF^{*} = 0.4$) leads to underestimation in OEF. Interestingly, the overestimation in estimated large $OEF^{\sharp}$ (i.e., $OEF^{\sharp} = 0.6$, $OEF^{*} = 0.45$ especially in occlusion case) in our study was different from the underestimation in estimated large $OEF^{\sharp}$ by Correia et al. and this may be caused by different methodologies used (steady-state or autoradiography).

To optimize the scan time for the $^{15}O_2$ scan, it is important to consider not only the error in OEF^{m} and $CMRO_2{}^{m}$ but also the error in CBF^{m} derived from the ^{15}O water scan, which is unavoidable factor. Considering the variation of OEF and $CMRO_2$, tissue heterogeneity, and applicability for clinical study, the optimal scan time of 3 min is suggested owing to following three reasons:

1. At the point of S/N of OEF and $CMRO_2$, the longer scan time is adequate (Fig. 3).
2. In terms of estimating OEF under circumstance of tissue heterogeneity, the longer scan time is adequate (Fig. 7a).
3. As shown in Fig. 7b, longer scan time has been required for $CMRO_2{}^{m}$ under the condition (iii). Conversely, shorter scan time has been required for $CMRO_2{}^{m}$ under the condition (i). The minimum error of $CMRO_2{}^{m}$ under the condition (ii) was achieved at the 180 s scan time.

Alpert et al. [18] earlier commented that factors of optimal scan time for oxygen-15-labeled water study are grouped as (1) the total observation time period, (2) scan and blood sampling protocol, and (3) the type and magnitude of tracer administration. This grouping can also be applied to oxygen-15 gas study, but most facilities have already installed the equipments, and it is not so easy to change the blood sampling protocol and supplement of tracer. In this study, we discussed the optimal scan time under the conditions of fixed administration dose, inhalation time, and blood sampling protocols. It must be noted that if administration protocol is changed from 1-min inhalation without breath control to others, present optimization of scan time may not be suited.

Recently, a rapid protocol with a single-PET scan with dual-tracer ($^{15}O_2$ and $H_2{}^{15}O$) administration method was developed [19, 20]. They employed integrated PET data for 90 s in H_2O phase and 180 s in O_2 phase. Our strategies to optimize the scan duration could be applied for this rapid protocol to estimate CBF, OEF, and $CMRO_2$ accurately.

Kobayashi et al. [21] examined relationship between count-based OEF and scan duration. They used quantitative OEF as a standard to evaluate optimal scan duration. Although their approach to obtain OEF is different from ours, as shown in this article, the tissue heterogeneity could be another important attribution for determining the optimal scan duration.

Conclusions

In this study, we performed computer simulation studies of $^{15}O_2$ gas inhalation protocol with the ARG method. Tissue heterogeneity largely affects the quantification of estimated OEF and $CMRO_2$, and is a dominant factor in the optimization of scan time in oxygen-15 gas study. According to these simulated results, the optimal scan time for $^{15}O_2$ gas inhalation protocol is suggested to be 3 min for ischemic disease.

Acknowledgments This study was supported in part by the Grant-in-Aid for Young Scientists (B) from the Ministry of Education, Culture, Sports, Science and Technology (19700395), Japan.

References

1. Ter-Pogossian MM, Herscovitch P. Radioactive oxygen-15 in the study of cerebral blood flow, blood volume, and oxygen metabolism. Semin Nucl Med 1985;15:377–94.
2. Baron JC, Bousser MG, Rey A, Guillard A, Comar D, Castaigne P. Reversal of focal "misery-perfusion syndrome" by extra-intracranial arterial bypass in hemodynamic cerebral ischemia: a case study with 15O positron emission tomography. Stroke 1981;12:454–9.
3. Gibbs JM, Wise RJ, Leenders KL, Jones T. Evaluation of cerebral perfusion reserve in patients with carotid-artery occlusion. Lancet 1984;11:310–4.
4. Mintun MA, Raichle ME, Martin WR, Herscovitch P. Brain oxygen utilization measured with O-15 radiotracers and positron emission tomography. J Nucl Med 1984;25:177–87.
5. Jones SC, Greenberg JH, Reivich M. Error analysis for the determination of cerebral blood flow with the continuous inhalation of 15O-labeled carbon dioxide and positoron emission tomograph. J Comput Assist Tomogr 1982;6:116–24.
6. Hatazawa J, Fujita H, Kanno I, Satoh T, Iida H, Miura S. Regional cerebral blood flow, blood volume, oxygen extraction fraction and oxygen utilization rate in normal volunteers measured by the autoradiographic and the single inhalation method. Ann Nucl Med 1995;9:15–21.
7. Kanno I, Iida H, Miura S, Murakami M. Optimal scan time of oxygen-15-labeled water injection method for measurement of cerebral blood flow. J Nucl Med 1991;32:1931–4.
8. Ito H, Shidahara M, Inoue K, Goto R, Kinomura S, Taki Y, et al. Effects of tissue heterogeneity on cerebral vascular response to acetazolamide stress measured by an I-123-IMP autoradiographic method with single-photon emission computed tomography. Ann Nucl Med 2005;19:251–60.
9. Kanno I, Iida H, Miura S, Murakami M, Takahashi K, Sasaki H, et al. A system for cerebral blood flow measurement using an $H_2{}^{15}O$ autoradiographic method and positron emission tomography. J Cereb Blood Flow Metab 1987;7:143–53.
10. Lammertsma AA, Jones T. Low oxygen extraction fraction in tumours measured with the oxygen-15 steady state technique: effect of tissue heterogeneity. Br J Radiol 1992;65:697–700.
11. Correia JA, Aplert NM, Buxton RB, Ackerman RH. Analysis of some errors in the measurement of oxygen extraction and oxygen consumption by the equilibrium inhalation method. J Cereb Blood Flow Metab 1985;5:591–9.
12. Iida H, Kanno I, Miura S, Murakami M, Takahashi K, Uemura K. A determination of the regional brain/blood partition coefficient of water using dynamic positron emission tomography. J Cereb Blood Flow Metab 1989;9:874–85.
13. Shidahara M, Watabe H, Kim KM, Oka H, Sago M, Hayashi T, et al. Evaluation of a commercial PET tomograph-based system for the quantitative assessment of rCBF, rOEF and $rCMRO_2$ by using sequential administration of ^{15}O-labeled compounds. Ann Nucl Med 2002;16:217–28.
14. Iida H, Jones T, Miura S. Modeling approach to eliminate the need to separate arterial plasma in oxygen-15 inhalation positron emission tomography. J Nucl Med 1993;34:1333–40.
15. Carson RE, Yan Y, Daube-Witherspoon ME, Freedman N, Bacharach SL, Herscovitch P. An approximation formula for the variance of PET region of interest values. IEEE Med Imaging 1993;12:240–50.
16. Watabe H, Endres CJ, Breier A, Schmall B, Eckelman WC, Carson RE. Measurement of dopamine release with continuous infusion of [11C]raclopride: optimization and signal-to-noise considerations. J Nucl Med 2000;41:522–30.
17. Strother SC, Casey ME, Hoffman EJ. Measuring PET scanner sensitivity: relating count rates to image signal-to-noise ratios using noise equivalent counts. IEEE Trans Nucl Sci 1990;37:783–8.
18. Alpert N. Optimization of regional cerebral blood flow measurements with PET (comment on J Nucl Med 1991;32:1931–4). J Nucl Med 1991;32:1934–6.
19. Kudomi N, Hayashi T, Teramoto N, Watabe H, Kawachi N, Ohta Y, et al. Rapid quantitative measurement of $CMRO_2$ and CBF by dual administration of ^{15}O-labeled oxygen and water during a single PET scan-a validation study and error analysis in anesthetized monkeys. J Cereb Blood Flow Metab 2005;25:1209–24.
20. Kudomi N, Watabe H, Hayashi T, Iida H. Separation of input function for rapid measurement of quantitative $CMRO_2$ and CBF in a single PET scan with a dual tracer. Phys Med Biol 2007;52:1893–908.
21. Kobayashi M, Kudo T, Tsujikawa T, Isozaki M, Arai Y, Fujibayashi Y, et al. Shorter examination method for the diagnosis of misery perfusion with count-based oxygen extraction fraction elevation in ^{15}O-Gas PET. J Nucl Med 2008;49:242–6.

Ann Nucl Med (2008) 22:549–556
DOI 10.1007/s12149-008-0170-z

ORIGINAL ARTICLE

Three-dimensional SPECT reconstruction with transmission-dependent scatter correction

Antti Sohlberg · Hiroshi Watabe · Hidehiro Iida

Received: 26 March 2007 / Accepted: 8 January 2008

Abstract
Objective The quality of single-photon emission computed tomography (SPECT) imaging is hampered by attenuation, collimator blurring, and scatter. Correction for all of these three factors is required for accurate reconstruction, but unfortunately, reconstruction-based compensation often leads to clinically unacceptable long reconstruction times. Especially, efficient scatter correction has proved to be difficult to achieve. The objective of this article was to extend the well-known transmission-dependent convolution subtraction (TDCS) scatter-correction approach into a rapid reconstruction-based scatter-compensation method and to include it into a fast 3D reconstruction algorithm with attenuation and collimator-blurring corrections.
Methods Ordered subsets expectation maximization algorithm with attenuation, collimator blurring, and accelerated transmission-dependent scatter compensation were implemented. The new reconstruction method was compared with TDCS-based scatter correction and with one other transmission-dependent scatter-correction method using Monte Carlo simulated projection data of ^{99m}Tc-ECD and ^{123}I-FP-CIT brain studies.
Results The new reconstruction-based scatter compensation outperformed the other two scatter-correction methods in terms of quantitative accuracy and contrast measured with normalized mean-squared error, gray-to-white matter and striatum-to-background ratios, and also in visual quality. Highest accuracy was achieved when all the corrections (i.e., attenuation, collimator blurring, and scatter) were applied.
Conclusions The developed 3D reconstruction algorithm with transmission-dependent scatter compensation is a promising alternative to accurate and efficient SPECT reconstruction.

Keywords Statistical reconstruction · Scatter correction · Collimator-blurring correction · Attenuation correction

A. Sohlberg · H. Watabe · H. Iida (✉)
National Cardiovascular Center Research Institute,
5-7-1 Fujishiro-dai, Suita, Osaka 565-8565, Japan
e-mail: iida@ri.ncvc.go.jp

Introduction

The qualitative and quantitative accuracy of single-photon emission computed tomography (SPECT) is hampered by attenuation, collimator blurring, and scatter. Whereas attenuation and collimator blurring can nowadays be corrected in clinically acceptable times, accurate and efficient scatter correction has been proved to be a more difficult problem even though scatter compensation has received a lot of attention over the past two decades.

Scatter-correction methods can generally be divided into two groups: projection- and reconstruction-based methods. In the projection-based methods, scatter correction is usually performed by subtracting the scatter contribution from the projection data before the actual reconstruction [1]. These methods differ in how the scatter contribution is determined. The projection-based methods are usually easy to implement and fast to execute, but the overall improvement in image quality achieved with the scatter compensation, is often reduced by the noise increase in the reconstructed images owing to the subtraction procedure. The reconstruction-based scatter-correction methods, on the other hand, include the effects of scatter into the forward- and backprojec-

tors of the reconstruction algorithm without direct scatter subtraction. The reconstruction-based methods have been shown to achieve greater accuracy and lower noise level than the projection-based methods [2, 3], but they are often unsuitable for clinical practice owing to unacceptably long execution times because scatter calculations have to be repeated at each iteration of the reconstruction algorithm.

One promising projection-based scatter-correction method that has received a lot of attention is the transmission-dependent convolution subtraction (TDCS) algorithm [4]. TDCS has been used by our group to correct scatter in cerebral blood flow [5] and dopamine transporter [6] quantitation studies. Despite the relatively good performance of TDCS in the aforementioned experiments, TDCS is still hampered by the fact that as a projection-based scatter-correction method it relies on scatter subtraction, and also by the fact that it needs geometric mean (GM) projection data, which for example renders accurate collimator-blurring correction impossible.

Even though the traditional TDCS scatter correction has its limitations, the transmission-dependent scatter-modeling approach, when included in reconstruction-based scatter-compensation method, might prove to be useful. Hutton et al. [7, 8] used transmission-dependent scatter modeling to generate scatter projections, which could be included in iterative reconstruction algorithm to perform reconstruction-based scatter compensation in their two-step reconstruction procedure. In this method, Hutton first reconstructed a "scatter-free" image using broad-beam attenuation map. This image was then used as an input for a transmission-dependent scatter-modeling algorithm to calculate scatter projections, which were finally used as a constant additive term in the final "scatter-corrected" reconstruction according to the method of Bowsher and Floyd [9]. The objective of our work was to extend the two-step transmission-dependent scatter correction by Hutton to a "more natural" single-step scatter-compensation method and to include it into a fast 3D reconstruction algorithm with attenuation and collimator-blurring corrections. We also compared our new reconstruction method with Hutton's method and also with conventional TDCS scatter-correction approach in terms of quantitative accuracy, contrast, and image quality.

Materials and methods

Implementation of the reconstruction algorithms

The attenuation, collimator blurring, and scatter correction were implemented into ordered subsets expectation maximization (OSEM) algorithm [10]. The OSEM is given by

$$f_j^{new} = \frac{f_j^{old}}{\sum_{i \in S_n} a_{ij}} \sum_{i \in S_n} a_{ij} \frac{p_i}{\sum_k a_{ik} f_k^{old}}, \quad (1)$$

where f is the reconstructed image, p the measured projections, j (or k) reconstruction voxel index, i projection pixel index, a_{ij} the probability that emission from voxel j is detected in pixel i, and S_n the nth subset. The image update in OSEM consists of sequential forward- and backprojection operations. The estimated projections are obtained by forwardprojecting the current image estimate ($\sum_k a_{ik} f_k^{old}$) and correction terms that are used to update the old image are formed by backprojecting the ratio of the measured and estimated projections ($\sum_{i \in S_n} a_{ij} \frac{p_i}{\sum_k a_{ik} f_k^{old}}$).

Here, the forward- and backprojectors were implemented as rotation based [11] (Fig. 1a), which makes attenuation, collimator blurring, and scatter correction relatively straightforward to perform. Attenuation correction factors for each voxel were calculated simply by summing the rotated attenuation map along columns. Collimator blurring, on the other hand, was modeled by convolving each plane of the reconstruction matrix parallel to the projection plane with a collimator response kernel, which was spatially invariant in that plane (Fig. 1b) [12]. The collimator response function was assumed to be a 2D Gaussian function, whose full width at half maximum (FWHM) is linearly dependent on the distance (d_{col}) from the plane to the collimator

$$\mathrm{FWHM}(d_{col}) = \alpha + \beta d_{col}, \quad (2)$$

Scatter modeling was implemented by slightly modifying the method presented by Hutton et al. [7, 8]. Hutton's method applies the rotating projectors and it compensates scatter as follows:

1. At each projection angle a "scatter-free" image, which has been obtained with reconstruction of the measured projection data using broad-beam attenuation coefficients, is first multiplied with monoexponential scatter kernel ($e^{-\alpha(d_{tis})}$), whose slope (α) is dependent on depth (d_{tis}) in tissue. A single scatter kernel is used for each plane at different tissue depth (see Fig. 1b).
2. Each point on each plane is then scaled with a transmission-dependent scatter-to-primary scatter fraction $SF_{S/P}$:

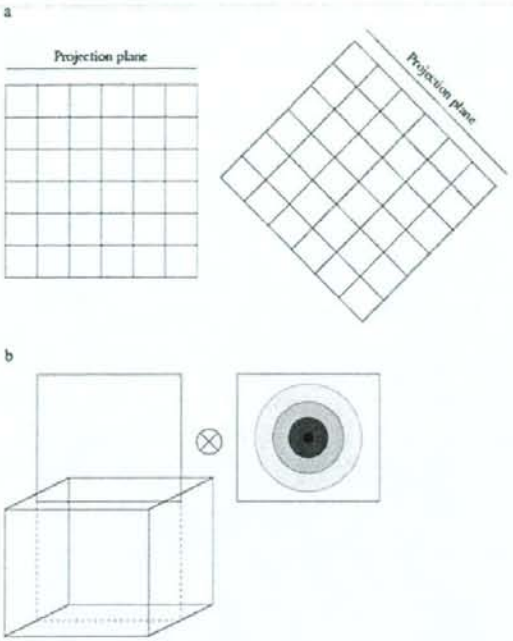

Fig. 1 a At each projection angle (two projection angles are shown), the rotating projector rotates the reconstruction matrix (single transverse plane is shown) so that its front face is aligned with the projection plane. The projections can be calculated simply by summing along columns of the reconstruction matrix. b Collimator response and scatter response modeling are realized by convolving each plane of the rotated reconstruction matrix (3D view is shown) parallel to the projection plane with an appropriate kernel

$$SF_{S/P} = A - B\left[e^{-\sum_{k=j}^{\text{skin}} \mu_k \Delta}\right]^{\gamma} - 1, \tag{3}$$

where A, B, and γ are the coefficients obtained from measurement [4], μ_k is the linear attenuation coefficient for voxel k and Δ voxel size.

3. The convolved and scaled voxel values are finally forwardprojected for obtaining scatter projection for the current projection angle.
4. After all the scatter projections are available, a new reconstruction is started. In this final reconstruction, the scatter projections obtained in the previous step are held as a constant term (s), which is added to the calculated projections $\left(\sum_k a_{ik} f_k^{\text{old}} + s\right)$.

Our new method differs from Hutton's method by the fact that it does not use a pre-reconstructed broad-beam attenuation coefficient image to calculate the scatter projections, but instead we perform the convolution and scatter-fraction scaling using the current image estimate (f_j^{old}). Therefore, our scatter compensation can be presented as

1. In the forwardprojection step of the OSEM algorithm at each projection angle the current image estimate (f_j^{old}) is convolved with the scatter kernels.
2. Each point on each plane is then scaled with the transmission-dependent scatter fraction.
3. The convolved and scaled voxel values are finally forwardprojected and added to the forwardprojected primary counts.

We believe that our approach leads to more natural scatter compensation, reduces user intervention and execution time.

Scatter modeling makes reconstruction time consuming and therefore we used coarse-grid modeling [13] to provide further improvement in speed. In coarse-grid scatter modeling, scatter compensation is performed using larger voxel size than the actual reconstruction voxel size (in our case scatter was calculated using a 64 × 64 × 64 matrix in the case of a 128 × 128 × 128 reconstruction matrix). It is also worth pointing out that our method models scatter only in the forwardprojection step and do not use collimator-blurring compensation in scatter estimation.

The conventional TDCS was implemented according to Meikle et al. [4] using a single exponential convolution kernel and scatter-to-total scatter fractions ($SF_{S/T}$)

$$SF_{S/T} = \frac{1}{A - Bt_i^{\beta/2}}, \tag{4}$$

where t_i is transmission factor for projection pixel i. Convolution with the depth-independent scatter kernel ($e^{-\alpha r}$) was performed to the measured projections (p_{meas}) after taking the GM and the result was scaled with the scatter fraction. The resulting scatter projections were subtracted from the measured projections for obtaining "scatter-free" projections (p_{nosc}):

$$p_{\text{nosc}} = p_{\text{meas}} - SF_{S/T}(p_{\text{meas}} \otimes e^{-\alpha r}). \tag{5}$$

The scatter-free projections were finally reconstructed using OSEM.

Reconstruction al gorithm calibration

The parameters needed for collimator blurring and scatter correction were obtained from Monte Carlo simulations with the SIMIND simulator [14]. A low-energy